Langmuir Turbulence in the Arctic Ocean: Insights From a Coupled Sea Ice –Wave Model

Aikaterini Tavri[1], Chris Horvat[1], Brodie Pearson[2], Guillaume Boutin[3], Anne Hansen[2], and Ara Lee[2]

[1]Brown University, Providence, RI, USA
[2]Oregon State University, Corvallis, OR, USA
[3]Nansen Environmental and Remote Sensing Center and Bjerknes Centre for Climate Research, Bergen, Norway

Correspondence: Aikaterini Tavri aikaterini_tavri@brown.edu

Abstract. Upper-ocean mixing regulates the vertical transport of heat, momentum, and tracers in the ocean surface boundary layer, yet its representation under sea ice remains highly uncertain. Langmuir turbulence (LT), generated by the interaction of wind stress and wave-induced Stokes drift, is a dominant open-ocean mixing mechanism and has been observed in leads, polynyas, and the marginal ice zone (MIZ), but its Arctic-wide occurrence and modulation by sea ice and waves are poorly constrained. Here we present the first pan-Arctic assessment of LT potential using a fully coupled sea ice–wave modeling framework integrating *neXtSIM* and *WAVEWATCH III*. Combining wind–wave forcing metrics with mixed-layer–integrated dissipation and vertical kinetic energy diagnostics, we show that LT-relevant forcing beneath sea ice is spatially confined and strongly intermittent. Conditions capable of sustaining LT occur primarily within the seasonal MIZ and arise episodically during late melt and freeze-up, rather than as a persistent background state. Sea ice concentration regulates the mean balance between wave- and shear-driven turbulence, while ice mechanical state, wave properties, and wind–wave misalignment control the efficiency of Langmuir-driven vertical motions without altering the underlying mixing regimes. As a result, LT in the Arctic MIZ most often coexists with wind-driven shear in mixed-forcing regimes, highlighting the need for regime-aware representations of upper-ocean mixing in climate models.

1 Introduction

The Arctic Ocean has traditionally been considered a region of weak upper-ocean mixing, primarily due to extensive sea ice cover that insulates the ocean from atmospheric forcing and dissipates wave energy (Morison et al., 1985; Pinkel, 2005). Under these conditions, turbulent exchange in the ocean surface boundary layer (OSBL) remains strongly suppressed, and vertical mixing occurs only during sporadic shear-driven and convective events. In recent decades, the rapid decline in sea ice, marked by the loss of multiyear ice, earlier seasonal melt onset, and expansion of open water area, has increasingly exposed the Arctic Ocean to wind and wave forcing, fundamentally shifting the traditional view (Stopa et al., 2016; Armitage et al., 2017; Muilwijk et al., 2024). These changes have amplified air–sea momentum transfer (Rainville et al., 2011; Dosser and Rainville, 2016) and expanded the Marginal Ice Zone (MIZ), a transitional region characterized by discontinuous ice cover that enables surface wave propagation and interaction with the floe field (Collins et al., 2018; Boutin et al., 2020).

Within the MIZ, surface gravity waves play a central role in mediating air–sea interaction. They modulate sea ice breakup and accelerate melt through enhanced mechanical stress and turbulent mixing (Thomson and Rogers, 2014; Thomson, 2022). Beyond direct wave breaking, surface waves also generate upper-ocean turbulence through Langmuir turbulence (LT), that develops when wind-forced shear aligns with wave-induced Stokes drift (Craik and Leibovich, 1976; Leibovich, 1983; McWilliams et al., 1997). LT forms coherent, counter-rotating Langmuir cells that vertically redistribute heat, momentum, and tracers, (Skyllingstad and Denbo, 1995; Kukulka et al., 2013; D'Asaro, 2014; Gargett and Grosch, 2014), and it has emerged as a key regulator of mixed layer dynamics in the open ocean (Belcher et al., 2012; Yang et al., 2014). The absence of LT parameterizations in ocean general circulation models contributes to systematic biases in mixed layer depth and sea surface temperature, particularly in wind- and wave-active regions such as the Southern Ocean (Belcher et al., 2012; Li et al., 2019).

Large eddy simulation (LES) studies show that LT deepens the mixed layer and enhances vertical entrainment fluxes by up to an order of magnitude compared to shear-driven turbulence alone, while also moderately increasing momentum fluxes (McWilliams et al., 1997; Sullivan et al., 2007). Enhanced vertical mixing leads to elevated turbulent kinetic energy (TKE) and stronger entrainment across density interfaces (Polton and Belcher, 2007; Pearson et al., 2015; Ali et al., 2019). These insights have motivated the development of new LT parameterizations for large-scale models that incorporate wave–current interactions and Stokes production terms (Van Roekel et al., 2012; Harcourt, 2015; Li and Fox-Kemper, 2017). Despite these advances, existing parameterizations have not been systematically evaluated in sea ice-covered regions, where the physical environment deviates substantially from typical open-ocean conditions due to the sea ice dynamics (McWilliams and Sullivan, 2000; Smyth et al., 2002; Brenner and Horvat, 2024).

In the Arctic, sea ice modifies upper ocean mixing dynamics in several ways. It limits wave fetch, alters the directional spread of wave energy, and attenuates short-wavelength wave components - all of which reduce the magnitude and vertical extent of Stokes drift (Ardhuin et al., 2016, 2020; Li and Fox-Kemper, 2017). Meanwhile, ice motion and floe interactions introduce additional sources of surface shear and turbulence (Skyllingstad and Denbo, 2001). Observations show that waves propagate long distances under sea ice and significantly influence mixing near leads, polynyas, and the ice edge (Drucker et al., 2003; Kirillov et al., 2013; Horvat et al., 2020; Cooper et al., 2022). The presence of Langmuir cells in sea ice openings, confirms that the LT mechanism remains active in ice-covered waters, albeit with intermittent occurrence and modified structure (Dethleff and Kempema, 2007; Voermans et al., 2019). Although prior studies on wave - ice interactions have primarily focused on mechanical breakup of sea ice (Collins et al., 2018; Squire, 2018), the turbulent mixing contributions of LT in sea ice covered regions remain largely unexplored. Recent modeling studies have incorporated wave - ice interactions to investigate localized upper-ocean mixing (Horvat et al., 2016; Manucharyan and Thompson, 2017; Cooper et al., 2022; Brenner and Horvat, 2024; Lo Piccolo et al., 2024), but no study has yet conducted a basin-wide, systematic evaluation of LT mixing potential under realistic Arctic sea ice and wave conditions.

In this study, we use a coupled sea ice - wave model that combines the neXtSIM Lagrangian sea ice model (Rampal et al., 2016) with the WAVEWATCH III (WW3) spectral wave model (Tolman et al., 2009). This modeling framework resolves surface Stokes drift, wave energy, and wind stress under evolving sea ice conditions. Using this information, we conduct an Arctic-wide assessment of LT potential under realistic wave - sea ice interaction. *LT potential* is defined as the amplitude of

Langmuir forcing inferred from surface shear (friction velocity, u_*) and surface wave-induced Stokes drift ($u_{s(0)}$), independent of oceanic dynamical adjustment. Our primary objective is to identify when and where LT mixing-supporting conditions emerge and persist, particularly in relation to seasonal sea ice advance and retreat. To quantify the role of wind–wave coupling, we compute both the standard (turbulent) Langmuir number La_t and the projected Langmuir number La_{proj}, incorporating the orientation angle α_{LOW} of Van Roekel et al. (2012), which represents the empirically derived rotation of Langmuir cells toward the combined Eulerian and Stokes contributions. Using these metrics, we map surface turbulent mixing regimes across space and time and estimate the seasonal evolution of TKE dissipation and vertical kinetic energy (VKE) associated with LT in the Arctic.

Section 2 details the coupled model configuration, the formulation of LT-relevant parameters, and an evaluation of the model inputs underpinning the LT metrics. Section 3 beginning with an assessment of LT-relevant wind and wave forcing in sea ice. We then map the spatial and temporal organization of upper-ocean mixing regimes and their variability across the Arctic, before examining seasonal and regional patterns in turbulent dissipation and normalized VKE. Finally, we assess the influence of wind - wave misalignment on LT energetics, highlighting where projected Langmuir diagnostics diverge from canonical estimates. Section 4 discusses the implications of our findings for Arctic mixed layer dynamics and model development and outlines key limitations of the study.

2 Data and Methods

2.1 The neXtSIM- WAVEWATCH III coupled model

We use a coupled sea ice - wave modeling framework that integrates the Lagrangian neXt-generation Sea Ice Model (neXtSIM) with the WAVEWATCH III (WW3) spectral wave model using the OASIS-MCT coupler (Boutin et al., 2021). NeXtSIM provides the evolving sea ice concentration, thickness, and floe-size distribution (FSD) that govern wave attenuation and the directional filtering of wave energy. Unlike Eulerian models, neXtSIM employs a moving triangular mesh, undergoing periodic local remeshing to retain a nominal resolution equivalent to the 25 km stereographic grid used by WW3. Although the two components do not share the same mesh, fields are exchanged every 30 minutes via interpolation onto the WW3 exchange grid. NeXtSIM receives atmospheric forcing from the European Centre for Medium-Range Weather Forecasts (ECMWF) fifth generation reanalysis (ERA5) and oceanic forcing from the Global Ocean Physics GLORYS12V1 reanalysis, but it does not employ lateral boundary conditions for sea ice. Ice drifts freely across the open boundaries, with inflow treated as if external ice properties match those adjacent to the boundary (Ólason et al., 2025).

WW3 simulates wave propagation and attenuation in sea ice using the IS2+IC2 attenuation scheme, which combines scattering, inelastic flexure, and under-ice friction (Boutin et al., 2018). The southern boundary of the regional WW3 domain is set at 54°N, and lateral wave spectra are prescribed along this open boundary using the Ifremer global WW3 Modélisation et Analyse pour le Recherche Côtière (MARC) hindcast. WW3 is forced with the same hourly ERA5 winds used to force neXtSIM, but as in standard WW3 configurations, no ocean currents are applied, neglecting wave–current interactions. This

configuration has been shown to reproduce realistic wave-in-ice behaviour in the Barents and Beaufort Seas (Ardhuin et al., 2018) and yields MIZ extents consistent with ICESat-2 altimeter observations (Boutin et al., 2022).

Our simulations cover the pan-Arctic domain for 2018–2022, with three-hourly output from the coupled neXtSIM–WW3 model. This framework does not include a prognostic ocean mixed layer, surface waves do not feed back on stratification or vertical redistribution of turbulence. All Langmuir-related metrics presented here therefore represent the potential for mechanically forced Langmuir turbulence implied by surface forcing, rather than the fully realized upper-ocean response. The oceanic stratification and mixed layer depth (MLD) used in subsequent energetic diagnostics are prescribed independently from the GLORYS12V1 reanalysis, rather than evolving prognostically within the coupled system. This analysis thus quantifies the spatial structure of Langmuir-driven mixing implied by surface forcing alone. This definition is analogous to the Langmuir forcing framework of Li et al. (2019) and captures relative patterns of Langmuir activity even when absolute dissipation rates are not explicitly resolved.

The coupled model provides key advantages over methods that only combine sea ice fields with ERA5 waves or rely on empirical Stokes drift formulations (Webb and Fox-Kemper, 2011). In neXtSIM–WW3, Stokes drift and wave radiation stress are computed directly from the ice-attenuated wave spectrum, rather than assuming open ocean conditions. Moreover, the prognostic FSD in neXtSIM modulates wave attenuation in a physically consistent manner, allowing the wave field to respond to floe fragmentation and the evolving seasonal morphology of the ice cover. By contrast, ERA5 treats sea ice as land above a concentration threshold and therefore cannot capture attenuation, directional filtering, or the associated modulation of Stokes drift, processes that exert strong control on Langmuir forcing in the MIZ. Both models use the same physical parameters as the reference configuration described in Boutin et al. (2022). Table S1 in the Supplementary Material lists the wave, wind, sea ice, and surface ocean variables used in this study, either directly from model output or computed from established physical relationships.

2.2 Evaluation of model inputs relevant to LT metrics

To assess the fidelity of the neXtSIM–WW3 inputs most relevant for LT diagnostics, we evaluate the surface winds, surface shear, Stokes drift, and the representation of heterogeneous sea ice and MIZ conditions. ERA5 winds, which force both neXtSIM and WW3, exhibit increased uncertainty under strong wind and high-latitude conditions, particularly near sharp ice–open-water transitions. Consistent with this, comparison against Cross-Calibrated Multi-Platform (CCMP) v3.1 data shows that ERA5 winds are systematically weaker than satellite-derived winds, and that this bias propagates directly into the diagnosed friction velocity u_*. Over 2018–2022, area-weighted Arctic mean 10-m winds exhibit a mean bias of -1.46 m s^{-1} (ERA5–CCMP), an RMSE of 1.47 m s^{-1}, and a correlation of 0.99 (Fig. S1), indicating high fidelity in synoptic variability despite a low mean state bias. Because CCMP assimilates ERA5 as a background field, this comparison primarily constrains mean state uncertainty.

The fidelity of neXtSIM sea ice concentration, ice-edge location, and deformation has been demonstrated in multiple studies. Ólason et al. (2025) report pan-Arctic sea ice extent RMSE of 0.76×10^6 km^2 and show that neXtSIM reproduces observed

patterns of ice drift and deformation from OSI-SAF products, supporting its ability to represent heterogeneous ice fields that modulate wave penetration and Stokes drift pathways.

Accurate estimation of Stokes drift $u_{s(0)}$ further depends on realistic representation of short-wave attenuation in ice. The IS2+IC2 attenuation scheme implemented in WW3 has been shown to reproduce observed wave decay and spectral evolution in the Beaufort MIZ (Ardhuin et al., 2018), and to yield realistic pan-Arctic MIZ extents and wave-affected ice regimes consistent with ICESat-2–derived freeboard variability and floe-scale ice properties (Boutin et al., 2022). Based on sensitivity analyses and independent observational constraints, prior studies indicate that residual uncertainty in the short-wave spectrum, and hence in inferred Stokes drift, is dominated by uncertainties in wind forcing and sea ice concentration, with magnitude on the order of tens of percent rather than order-unity errors (Ardhuin et al., 2018; Boutin et al., 2022).

2.3 Surface stress partitioning and wind–wave forcing

To characterize momentum input into the ocean mixed layer under partial ice cover, we compute an effective surface stress that partitions momentum between the ice–ocean and atmosphere–ocean interfaces. Following the framework of Brenner et al. (2021), the net ocean surface stress is defined as an area-weighted combination of ice–ocean and atmosphere–ocean stresses, scaled by the local sea ice concentration:

$$\boldsymbol{\tau}_{ocn} = A\,\boldsymbol{\tau}_{io} + (1 - A)\,\boldsymbol{\tau}_{ao} \tag{1}$$

where A is the sea ice concentration (0 = open ocean, 1 = fully ice covered), and the direct atmosphere–ocean stress is given by:

$$\boldsymbol{\tau}_{ao} = \rho_a C_{ao}\,|\mathbf{u}_a|\,\mathbf{u}_a \tag{2}$$

with with ρ_a as air density, $\mathbf{u}_a$ the 10-m wind velocity, and C_{ao} the air–sea drag coefficient over open water. Subsequently, we define an effective water-side friction velocity u_*, which represents the shear strength associated with the net surface stress transmitted to the ocean under partial ice cover:

$$u_* = \sqrt{\frac{|\boldsymbol{\tau}_{ocn}|}{\rho_o}}. \tag{3}$$

where ρ_o is the density of seawater. It provides the fundamental scaling for wind-driven mixing processes. The net surface stress $\boldsymbol{\tau}_{ao}$ represents an upper bound on the momentum flux available to drive mixed-layer shear during periods of active wave growth. This primarily affects the absolute magnitude of the diagnosed friction velocity u_*, while its spatial structure and relative variability remain more robust.

In addition to wind shear, surface waves contribute momentum through Stokes drift, the net Lagrangian transport of water particles due to wave orbital motion. In WW3, the surface Stokes drift components (z = 0) are computed from the two-dimensional wave energy spectrum $F(k, \theta)$ as:

$$U_{sx}^{z=0} = g \int\int \frac{k^2 \cos(\theta)}{\sigma^2} F(k,\theta)\, d\theta\, dk, \tag{4}$$

and

$$U_{sy}^{z=0} = g \int\int \frac{k^2 \sin(\theta)}{\sigma^2} F(k,\theta)\, d\theta\, dk. \tag{5}$$

Here, σ is the wave frequency, k is the wave number and θ the propagation direction. These expressions define the eastward and northward components of the surface Stokes drift vector u_s. The effective friction velocity and surface Stokes drift combined, provide two primary dynamical inputs required to evaluate *the potential for LT* under varying sea ice conditions.

2.4 Langmuir turbulence metrics in the Arctic

The Langmuir number (La_t) is a widely used parameter for quantifying the relative contributions of wind stress and wave-induced Stokes drift to upper ocean turbulence (McWilliams and Sullivan, 2000). It is defined as:

$$La_t = \sqrt{\frac{u_*}{u_{s(0)}}}, \tag{6}$$

where u_* is the friction velocity associated with the effective surface stress applied to the ocean, and $u_{s(0)}$ is the surface Stokes drift magnitude. In the open ocean, typical values of La_t range between 0.2 and 0.5 (Belcher et al., 2012), suggesting strong wave influence and active Langmuir circulation development, although La_t can reach values near or above 1 when wave effects are weak and wind-driven processes dominate (McWilliams et al., 1997; Belcher et al., 2012). These ranges are consistent with results from LES and field observations showing that stronger LT and deeper mixing are associated with lower La_t (Harcourt, 2015). La_t is used in ocean modeling as a diagnostic of upper-ocean mixing regimes and to inform turbulence parameterizations. However, the traditional formulation implicitly assumes that the wind stress and Stokes drift are aligned. In realistic wave fields, especially in the Arctic, where mixed swell, turning winds, and ice-induced attenuation are common, misalignment can strongly reduce the effective Stokes shear that drives Langmuir circulations (Kukulka et al., 2010; Van Roekel et al., 2012; Li and Fox-Kemper, 2017).

To account for wind–wave misalignment, we adopt the *projected* Langmuir number of Van Roekel et al. (2012), which incorporates the dynamic orientation of the dominant Langmuir cells. In this framework, Langmuir cells do not necessarily align with the wind, but with the direction of maximum Lagrangian shear, set by a balance between Eulerian shear, Stokes drift, stratification, and Coriolis rotation. The dynamic orientation angle α_L represents the direction of the dominant Langmuir cells relative to the wind. Incorporating this angle yields the generalized projected Langmuir number:

$$La_{\mathrm{proj}} \equiv \left(\frac{|u_*| \cos(\alpha_L)}{|u_{s(0)}| \cos(\theta_{ww} - \alpha_L)} \right)^{1/2}, \tag{7}$$

where θ_{ww} is the angle between the wind stress and Stokes drift vectors. Equation (7) captures two effects: (i) the reduced wind-driven shear along the Langmuir cell axis via $\cos(\alpha_L)$, and (ii) the projected of Stokes forcing along that same axis via $\cos(\theta_{ww} - \alpha_L)$.

Direct evaluation of α_L requires resolving the vertical structure of the Lagrangian shear, which is not feasible at the $\sim 25\,\mathrm{km}$ resolution of our pan-Arctic model. We therefore use the low-order wave (LOW) approximation α_{LOW} proposed by Van Roekel et al. (2012), which provides an empirical estimate of Langmuir cell orientation by combining Eulerian shear and surface-layer Stokes shear:

$$\tan\alpha_{\mathrm{LOW}} \approx \frac{\langle \partial v_s/\partial z \rangle_{D_L}}{\langle -u_*/(\kappa z) + \partial u_s/\partial z \rangle_{D_L}}, \tag{8}$$

where angle brackets denote a depth average over the Langmuir-affected layer D_L, and κ is the von Kármán constant. LES results show that α_{LOW} captures the orientation of Langmuir cells over a wide range of wind–wave misalignment angles, making it suitable for large-scale applications.

In situations with strong wind–wave misalignment, α_{LOW} typically reduces the effective projection of the Stokes drift into the Langmuir cell direction, partially counteracting the muted Langmuir response obtained when misalignment is represented solely by θ_{ww}. Hence, in our analysis, we we substitute α_{LOW} for α_L in Eq. (7), yielding

$$La_{\mathrm{proj}} = \left(\frac{|u_*|\cos(\alpha_{\mathrm{LOW}})}{|u_{s(0)}|\cos(\theta_{ww} - \alpha_{\mathrm{LOW}})} \right)^{1/2}. \tag{9}$$

2.4.1 Surface forcing metrics and mixing regime classification

We introduce two complementary metrics to evaluate the potential for LT under partial sea ice cover. The first evaluates how frequently surface forcing beneath sea ice resembles open-water conditions, based on exceedance metrics for surface stress and wave forcing. The second classifies near-surface ocean conditions into discrete mixing regimes based on the Langmuir number La_t and tracks transitions between these regimes over space and time.

We define exceedance metrics to quantify how often the near-surface wind and wave forcing in ice-covered regions approaches values typical of open water. The two primary LT drivers considered are the surface friction velocity (u_*) and the surface Stokes drift velocity ($u_{s(0)}$). For each season (s) and grid cell (x, y), we define an open-water (OW) benchmark by computing the median value of a given variable X over all ice-free conditions (SIC < 0.15):

$$X_{\mathrm{OW}}^{(s)} = \mathrm{median}\{X_t(x,y) \,:\, \mathrm{SIC}_t(x,y) < 0.15,\, t \in s\}. \tag{10}$$

This benchmark represents the typical magnitude of atmosphere–ocean or wave-induced surface forcing under ice-free conditions during a given season.

At each ice-covered grid cell (SIC ≥ 0.15), we compute the fraction of time steps for which the local value exceeds the seasonal OW benchmark. For a single variable, the exceedance metric is defined as

$$\mathrm{Exceedance}_X^{(s)}(x,y) = \frac{N_t\left[\mathrm{SIC}_t(x,y) \geq 0.15 \,\wedge\, X_t(x,y) \geq X_{\mathrm{OW}}^{(s)}\right]}{N_t\left[\mathrm{SIC}_t(x,y) \geq 0.15\right]}, \tag{11}$$

where $N_t[\cdot]$ denotes the number of seasonal time steps satisfying the specified condition. Seasons follow meteorological definitions: winter (DJF), spring (MAM), summer (JJA), and fall (SON).

To isolate conditions most relevant for Langmuir turbulence, we further define a joint exceedance metric that quantifies the fraction of ice-covered time during which both surface friction velocity and surface Stokes drift simultaneously exceed their respective OW seasonal medians:

$$\mathrm{JointExceedance}^{(s)}(x,y) = \frac{N_t\left[\mathrm{SIC}_t(x,y) \geq 0.15 \ \wedge \ u_{*,t}(x,y) \geq u^{(s)}_{*,\mathrm{OW}} \ \wedge \ u_{s(0),t}(x,y) \geq u^{(s)}_{s(0),\mathrm{OW}}\right]}{N_t\left[\mathrm{SIC}_t(x,y) \geq 0.15\right]}. \tag{12}$$

These exceedance metrics provide a physically interpretable measure of the frequency and persistence of LT-relevant surface forcing in ice-covered regions, relative to open-ocean benchmarks.

To characterize the evolving balance between wind-driven and wave-driven mixing, we classify surface forcing into three distinct regimes based on the turbulent Langmuir number La_t (Li et al., 2019). At each time step T and grid cell (x,y), the regime is defined as:

$$\mathcal{R}(x,y,T) = \begin{cases} 1 & \text{if } La_t(x,y,T) > 0.94 \quad \text{(Shear-dominated)} \\ 2 & \text{if } 0.43 < La_t(x,y,T) \leq 0.94 \quad \text{(Mixed-forcing)} \\ 3 & \text{if } La_t(x,y,T) \leq 0.43 \quad \text{(Wave-dominated).} \end{cases} \tag{13}$$

To relate mixing regimes to sea ice conditions, we define spatial regions $\Omega(T)$ at each time step based on the local sea ice concentration $\mathrm{SIC}(x,y,T)$:

$$\Omega_{\mathrm{ice}}(T) = \{(x,y)\,|\,\mathrm{SIC}(x,y,T) > 0.8\}, \tag{14}$$

$$\Omega_{\mathrm{MIZ}}(T) = \{(x,y)\,|\,0.15 \leq \mathrm{SIC}(x,y,T) \leq 0.8\}, \tag{15}$$

$$\Omega_{\mathrm{OW}}(T) = \{(x,y)\,|\,\mathrm{SIC}(x,y,T) < 0.15\}. \tag{16}$$

For each region Ω and regime $r \in \{1,2,3\}$, we compute the spatial fraction of grid cells occupying regime r at time T as

$$f^{\Omega}_r(T) = \frac{1}{|\Omega(T)|} \sum_{(x,y)\in\Omega(T)} \delta(\mathcal{R}(x,y,T) = r)\,, \tag{17}$$

where $\delta(\cdot)$ is the indicator function and $|\Omega(T)|$ is the number of valid grid cells in region $\Omega(T)$.

Beyond regime occupancy, we assess the temporal stability of the surface forcing balance by tracking transitions between regimes. For each grid cell (x,y), we count transitions from regime r_n to r_m between successive time steps, restricted to periods when the grid cell remains within the same ice regime Ω:

$$T^{\Omega}_{r_n\to r_m}(x,y) = \sum_{T=2}^{T_{\max}} \delta(\mathcal{R}(x,y,T-1) = r_n)\,\delta(\mathcal{R}(x,y,T) = r_m)\,\delta((x,y) \in \Omega(T-1) \cap \Omega(T))\,. \tag{18}$$

Spatial differences in temporal sampling are evaluated using transition counts, normalized by the number of time steps a grid cell resides within region Ω,

$$\bar{T}^{\Omega}_{r_n\to r_m}(x,y) = \frac{T^{\Omega}_{r_n\to r_m}(x,y)}{N_{\Omega}(x,y)}, \tag{19}$$

where $N_\Omega(x,y)$ denotes the total number of time steps satisfying the regional criterion. The resulting normalized transition frequency provides a measure of how often the dominant surface forcing balance reorganizes at a given location over the analysis period.

2.4.2 Langmuir Turbulence Energetics

To examine how LT modifies upper-ocean energetics, we evaluate two complementary metrics derived from the vertically integrated turbulent kinetic energy (TKE) budget: (i) the mixed-layer–averaged vertical velocity variance, $\langle w'^2 \rangle_{H_{ML}}$, and (ii) the TKE dissipation rate, ε. Both are based on empirically derived LES scalings, but they characterize distinct aspects of the turbulent response.

We compute $\langle w'^2 \rangle_{H_{ML}}$ following the LES-based scaling of Van Roekel et al. (2012):

$$\langle w'^2 \rangle_{H_{ML}} = 0.6\,[u_* \cos(\alpha_{\mathrm{LOW}})]^2 \left(1 + (c_1 La_x)^{-2} + (c_2 La_x)^{-4}\right), \tag{20}$$

where u_* is the friction velocity and La_x denotes the Langmuir number metric used in the scaling. The La_x^{-2} and La_x^{-4} terms capture the nonlinear enhancement of vertical velocity variance by Langmuir forcing, with lower Langmuir numbers indicating stronger turbulence. The projection factor $\cos(\alpha_{\mathrm{LOW}})$ ensures that vertical velocity is appropriately scaled along the Langmuir cell axis. For the turbulent Langmuir number, we set $La_x = La_t$ and $\alpha_{\mathrm{LOW}} = 0$, corresponding to Langmuir cells aligned with the wind. We adopt $(c_1, c_2) = (3.1, 5.7)$ for La_t and $(c_1, c_2) = (3.1, 5.4)$ for La_{proj}, consistent with the original LES fits following Van Roekel et al. (2012). The scaling in Eq. (20) was derived under conditions of weak or destabilizing surface buoyancy flux in LES. Because Arctic mixed layers are frequently stabilized by ice melt and freshwater input, the diagnosed values of $\langle w'^2 \rangle_{H_{ML}}$ should be interpreted as a measure of LT potential, rather than as a direct prediction of the realized turbulent state.

The contribution of LT to upper-ocean energy dissipation is quantified using a vertically integrated turbulent kinetic energy (TKE) scaling framework following Belcher et al. (2012). In the mixed-layer interior, away from the near-surface wave-breaking region, the turbulent dissipation rate can be approximated as the sum of contributions from wind-driven shear, Stokes drift (Langmuir turbulence), and surface buoyancy forcing. Factoring out the shear-based velocity scale yields:

$$\varepsilon \sim \frac{u_*^3}{H_{\mathrm{ML}}} \left[A_s + A_L\, La_x^{-2} + A_c\, \frac{B_s H_{\mathrm{ML}}}{u_*^3} \right], \tag{21}$$

where H_{ML} is the mixed-layer depth, La_x is a Langmuir number metric characterizing the relative importance of wave forcing to shear, and B_s is the surface buoyancy flux. The constants A_s, A_L, and A_c are empirical coefficients of order unity that represent the efficiency of shear-, Langmuir-, and buoyancy-driven turbulence, respectively.

The Langmuir contribution in Eq. (21) scales as La_x^{-2}, reflecting the ratio of the Stokes drift velocity scale to the friction velocity, u_s/u_*. This scaling is consistent with the Langmuir velocity scale $w_{*L} = (u_*^2 u_s)^{1/3}$ and with LES results demonstrating enhanced interior mixing under strong wind–wave coupling (Belcher et al., 2012; Van Roekel et al., 2012).

Consistent with the surface forcing-only framework described in Section 2.1, we omit the buoyancy-dependent contribution in Eq. (21) and adopt a reduced formulation that isolates mechanically driven turbulence. We define a mechanically forced

dissipation scale as:

$$\varepsilon_{\mathrm{mech}} = \frac{u_*^3}{H_{\mathrm{ML}}}\left(1+\beta\, La_x^{-2}\right), \tag{22}$$

where the second term represents enhancement of turbulent dissipation by wave-induced Stokes drift. The empirical coefficient β parameterizes the efficiency with which LT augments mechanically driven dissipation under weakly stratified conditions. LES in open-ocean settings suggest $\beta \approx 0.15$. We emphasize that $\varepsilon_{\mathrm{mech}}$ is an energetic proxy rather than a full representation of turbulent dissipation, as it neglects buoyancy production, entrainment, and stratification-dependent suppression. Its purpose here is to quantify the spatial and temporal variability of mechanically mediated energy input associated with wind and wave forcing, providing a physically interpretable metric for comparing mixing regimes within the MIZ.

We adopt a reanalysis-derived mixed-layer depth H_{ML} as a physically consistent bulk depth scale rather than a real-time boundary-layer estimate. Specifically, we use the GLORYS12 reanalysis (0.08° resolution), computed daily and remapped to the 25 km model grid. Although GLORYS12 does not explicitly resolve ice-modified boundary-layer processes, its mixed-layer depth provides a physically grounded, spatially and seasonally varying vertical scale over which mechanically forced turbulence can be interpreted in a vertically integrated sense. Equation (22) is therefore interpreted as an effective dissipation scaling rather than a closed TKE budget, and is used here as a diagnostic of LT potential under wind–wave forcing.

3 Results

3.1 Spatiotemporal variability of surface forcing across the Arctic

Figure 1 presents the seasonal distribution of joint exceedance of open-water (OW)-like surface forcing over the five-year simulation period. Across all seasons, joint exceedance is generally low, with values rarely exceeding 0.2, indicating that conditions comparable to OW, where strong winds and waves act simultaneously, occur only infrequently in sea ice. Where it does occur, joint exceedance is spatially confined and predominantly concentrated along the seasonal sea ice edge. The highest values are consistently found in the Barents, Greenland, and Chukchi Seas, regions where ice cover is thinner, more mobile, and more frequently disrupted.

The spatial distribution exhibits clear seasonal contrasts. During winter and the transitional seasons (DJF, MAM, SON), joint exceedance is stronger and more spatially continuous along the MIZ, reflecting the increased likelihood of storm-driven conditions interacting with loosely consolidated ice. In contrast, summer (JJA) shows the weakest joint exceedance overall. However, exceedance events in summer are more geographically dispersed, suggesting that while LT-relevant forcing is rarer, it can still intermittently extend into areas classified as pack ice. This scattered summer signal highlights the potential for episodic Langmuir turbulence beyond the immediate MIZ during the melt season.

To provide additional physical context for this seasonal asymmetry, Supplementary Figure S2 summarizes the distribution of significant wave height (H_s) within the marginal ice zone (MIZ) across seasons. Winter (DJF) exhibits both the highest median wave heights and the largest spread, consistent with frequent storm-driven wave events capable of penetrating into partially ice-covered regions. In contrast, summer (JJA) wave heights are strongly suppressed, with low median values and

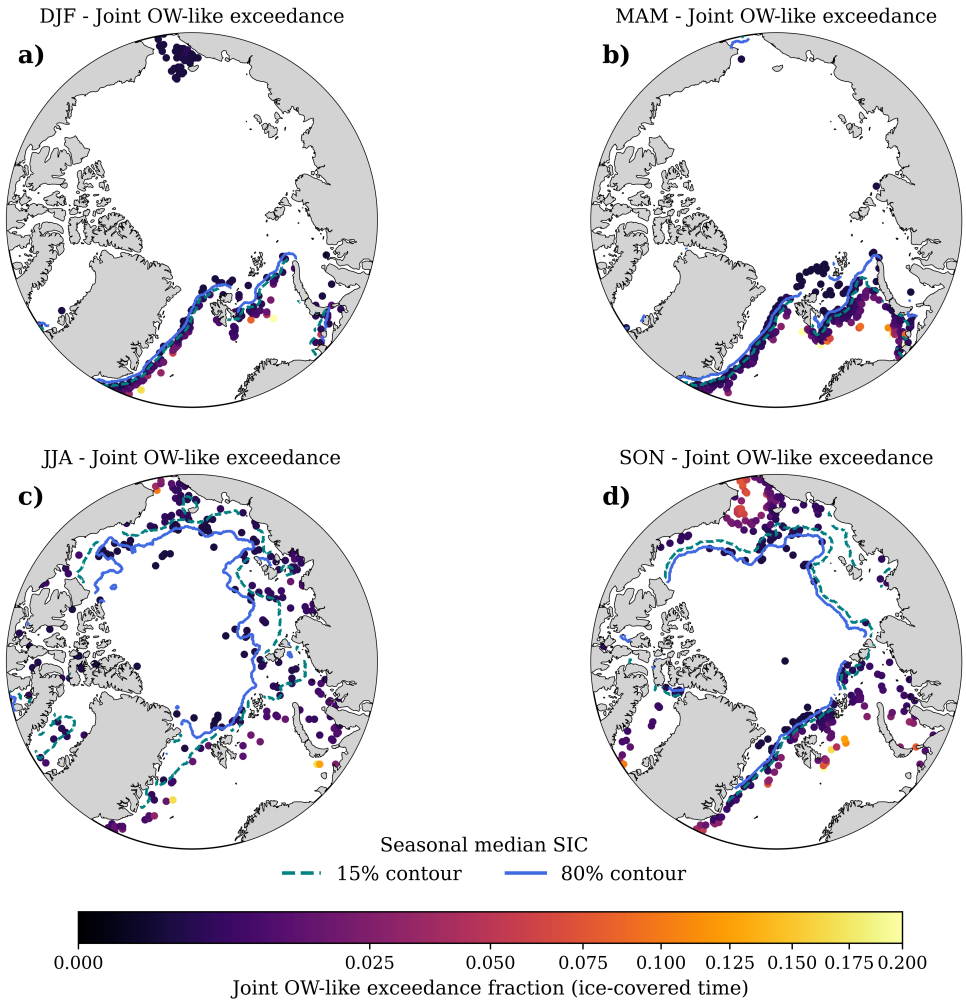

Figure 1. Seasonal joint exceedance of wind–wave surface forcing beneath Arctic sea ice. Panels (a–d) show, for each season, the fraction of under-ice time ($SIC \geq 0.15$) during which both surface friction velocity u_* and surface Stokes drift $u_{s(0)}$ simultaneously exceed their respective seasonal open-water medians ($SIC < 0.15$). Elevated values (yellow–orange) indicate locations where wind-driven shear and residual wave-driven drift intermittently reach open-water–like magnitudes despite the presence of sea ice. A nonlinear (power-law) color scaling is applied to enhance contrast at low exceedance fractions, emphasizing spatial variability in rare joint exceedance events. Dashed and solid contours denote the seasonal mean **15%** (teal) and **80%** (blue) sea ice concentration boundaries, respectively, providing context for the typical extent of the marginal ice zone and the transition to the consolidated pack. Joint exceedance is shown only at grid cells that experience sea ice conditions at least once during each season.

limited variability, consistent with reduced Stokes drift forcing even where ice cover is fragmented. The transitional seasons (MAM, SON) exhibit intermediate behavior, characterized by lower median wave heights but pronounced upper tails, reflecting episodic wave events rather than sustained wave forcing.

Consistent with seasonal wave climate, the confinement of joint exceedance to the MIZ across all seasons highlights the role of sea ice state in regulating surface forcing. Reduced joint exceedance during summer reflects both diminished storm activity and enhanced attenuation of wave-induced Stokes drift within even moderately concentrated ice, in agreement with theoretical and observational studies documenting rapid decay of Stokes transport under partial ice cover (Ardhuin et al., 2016; Herman, 2017; Liu and Mollo-Christensen, 1988). In contrast, the persistence of joint exceedance during winter and transitional seasons indicates that episodic storm-driven events can temporarily restore OW-like forcing beneath the ice, even when mean conditions remain ice covered.

3.2 Mapping upper-ocean mixing regime dynamics in the Arctic

To further explore the controls on LT potential, we examine the spatial and seasonal structure of the turbulent Langmuir number (La_t). All La_t medians are computed over the full spatial domain shown in Figure 2, without restricting the analysis based on sea ice concentration. The five-year climatological median (Figure 2a) reveals a persistent band of low La_t encircling the perennial ice pack and closely following the climatological 15% SIC contour and consistent with patterns shown in Figure 1. Elevated median La_t values (> 1) dominate the central Arctic under compact ice cover, indicating regimes where wave influence is weak and surface shear governs upper-ocean mixing. In contrast, moderate to low median La_t values (< 0.45), which indicate some LT potential, are confined to narrow, seasonally evolving bands along the ice edge. Under open-ocean conditions (SIC < 0.15), median La_t values are generally below 0.35, consistent with the range identified by Belcher et al. (2012) as favorable for LT conditions. This large-scale spatial structure reflects the progressive suppression of wave-induced Stokes transport with increasing ice concentration, as LT potential diminishes when Stokes production weakens relative to shear production. Seasonal medians (Figures 2b–e) further illustrate how transitions in ice state modulate the balance between wave and wind forcing. During winter and spring (Figures 2b–c), sharp gradients in La_t delineate the transition from wave-influenced conditions near the ice edge to shear-dominated regimes within the consolidated ice. This abrupt shift reflects compact ice cover and strong wave attenuation, which limit Stokes drift penetration beneath the ice even during periods of strong wind forcing. In contrast, summer and fall (Figures 2d–e) exhibit a broader and more continuous band of reduced La_t extending into the seasonal sea ice zone. Increased OW exposure, enhanced fetch, and elevated wave activity during these seasons allow Stokes drift to penetrate farther beneath the ice, reducing La_t and promoting conditions more conducive to LT. These seasonal patterns indicate that departures from open-ocean La_t values are primarily associated with modulation of Stokes drift by sea ice rather than changes in wind forcing alone. The seasonal MIZ therefore emerges as a dynamically distinct transition zone in which the balance between shear- and wave-driven turbulence shifts toward LT-favorable conditions, while the interior pack ice remains characterized by persistently shear-dominated mixing throughout the year.

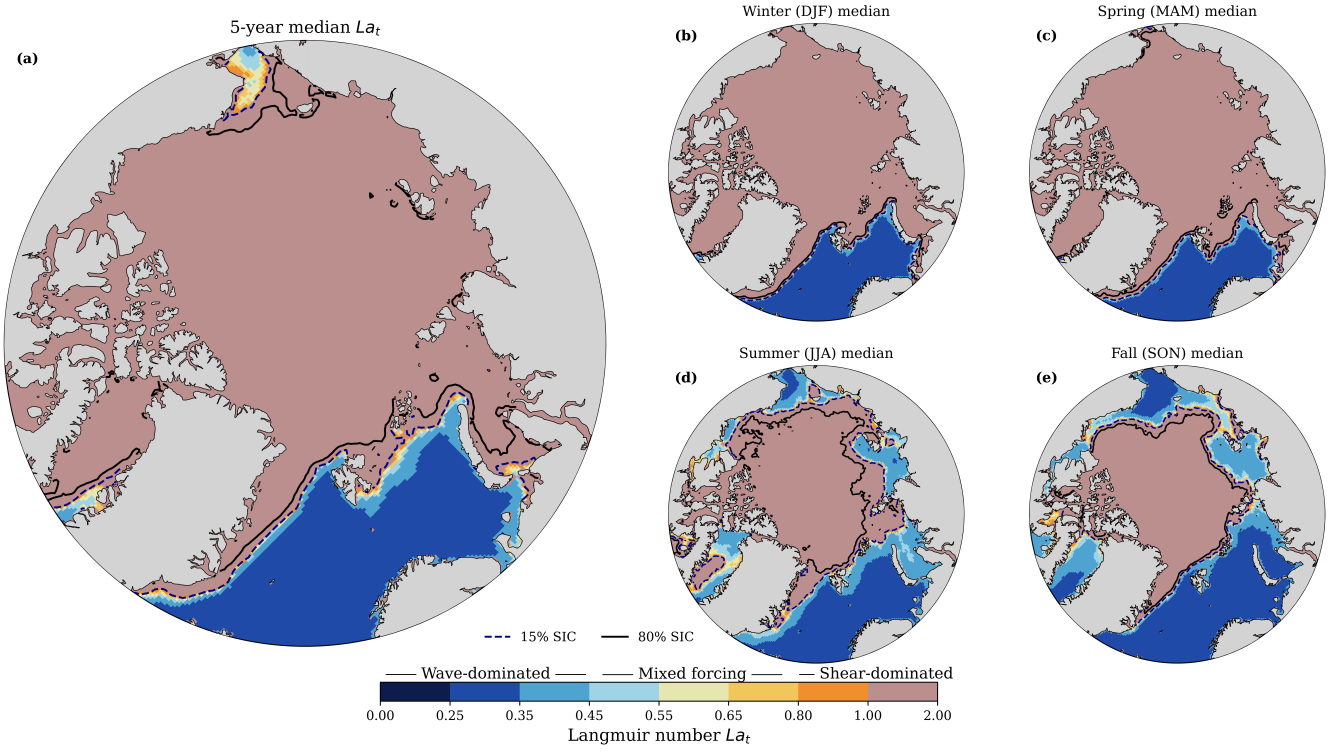

Figure 2. Spatial distribution of the median Langmuir number La_t, integrated over 2018 to 2022, along with its seasonal medians. Panel (a) shows the five-year climatological median of the Langmuir number La_t computed across all seasons. The median 15% and 80% SIC contours are overlaid in dark blue and black colors marking the median SIC-defined extent of the MIZ across seasons. Panels (b–e) show the medians for winter (DJF), spring (MAM), summer (JJA), and fall (SON), respectively. In all panels, La_t is shown for all ocean grid cells without applying a SIC mask; SIC contours are overlaid for context.

3.3 Mapping upper-ocean mixing regime dynamics in the Arctic

Figure 3 synthesizes the spatial structure, temporal variability, and persistence of upper-ocean mixing regimes under consistent sea ice concentration ($SIC > 15\%$) conditions. Panel (a) shows the dominant mixing regime at each grid cell, defined by $\geq$50% seasonal persistence and quantified using Eq. (13). The Arctic interior is characterized primarily by shear-driven mixing ($La_t \geq 0.94$), while mixed ($0.43 \leq La_t < 0.94$) and wave-driven ($La_t < 0.43$) regimes are confined to the MIZ and regions proximal to the ice edge, where surface-wave and wind forcing increasingly compete. Panel (b) maps the normalized frequency of regime transitions at each grid cell, expressed as the number of regime changes per ice-covered day. Enhanced regime instability is strongly localized to the MIZ, particularly along sectors exposed to episodic wave activity and intermittent open-water conditions. In contrast, the consolidated interior pack ice exhibits uniformly low transition rates, indicative of stable and persistent forcing balances throughout the year. The temporal evolution of regime instability within the MIZ is shown in panel (c), quantified as the fraction of MIZ grid cells ($0.15 \leq \text{SIC} \leq 0.8$) that undergo at least one regime transition within a 30-day

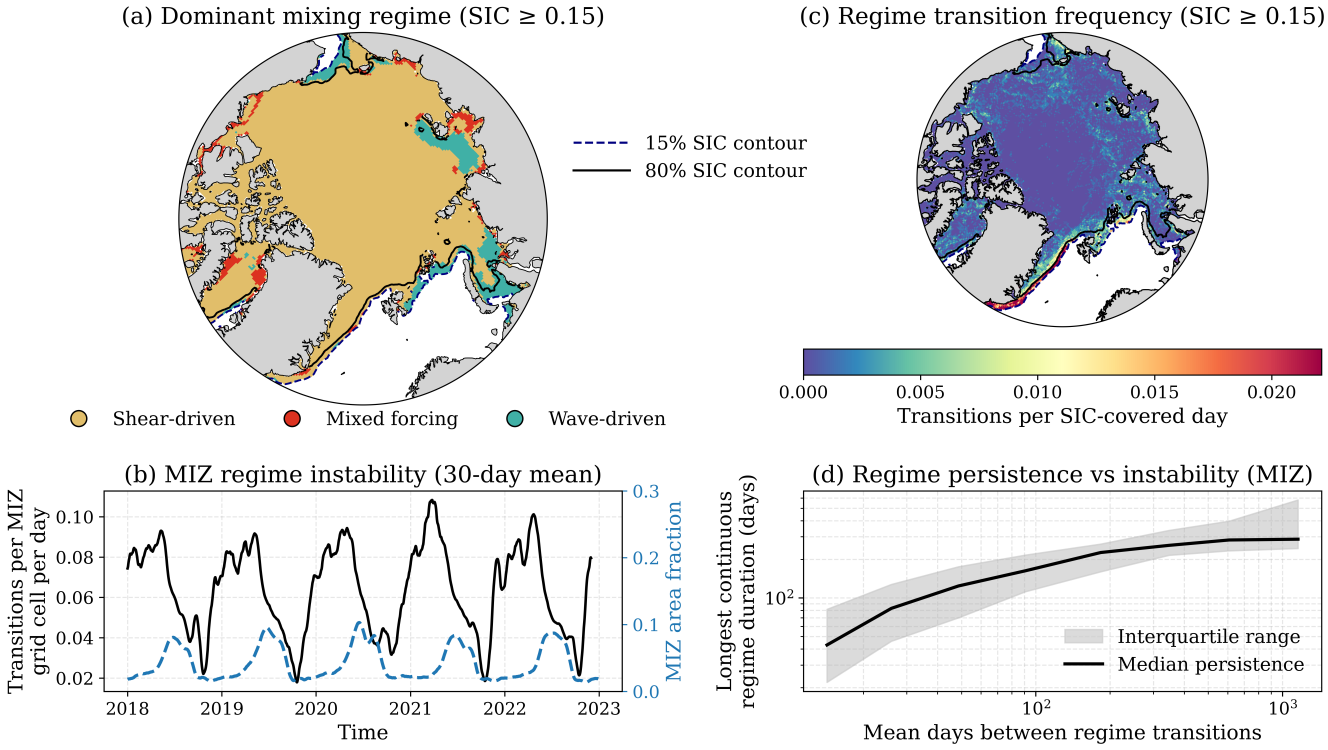

Figure 3. Spatial and temporal characteristics of upper-ocean mixing regime dynamics under sea ice for SIC $\geq$ 0.15. (a) Dominant mixing regime defined as the regime occupying at least 50% of SIC-covered days at each grid cell over the analysis period. Shear-driven conditions dominate the compact ice interior, while mixed and wave-driven regimes preferentially occur near the ice edge and in seasonally ice-covered regions. Dashed and solid contours indicate the 15% and 80% sea ice concentration (SIC) thresholds, respectively. (b) Normalized regime transition frequency (transitions per SIC-covered day) for SIC $\geq$ 0.15, highlighting enhanced temporal variability along the MIZ and reduced variability within the compact ice interior. (c) Time series of marginal ice zone (MIZ; 0.15 $\leq$ SIC $\leq$ 0.8) regime instability, defined as the fraction of MIZ grid cells undergoing at least one regime transition within a 30-day window (black), together with the contemporaneous fraction of the Arctic domain classified as MIZ (blue, dashed). (d) Relationship between regime persistence and instability within the MIZ, shown as the median longest continuous regime duration (black) and interquartile range (shading) binned by the mean number of days between regime transitions. Increasing transition frequency is associated with a systematic reduction in regime persistence.

window. Regime instability exhibits pronounced seasonal modulation, with recurrent peaks during periods of ice advance and retreat. Peaks in regime instability systematically precede maxima in MIZ area, indicating a temporal lag between dynamic reorganization and the geometric expansion of the SIC-defined MIZ. Periods of elevated instability correspond to times when grid cells reside near regime boundaries and experience strong competition between wind-, wave-, and ice-mediated forcing, whereas subsequent MIZ expansion reflects the integrated outcome of this reorganization. Panel (d) directly links regime instability to persistence by relating the mean time between regime transitions to the longest continuous duration of a single regime within MIZ grid cells. Median regime persistence increases monotonically with increasing time between transitions,

however the relationship is highly non-linear, with persistence collapsing rapidly once transitions become more frequent. In our analysis, this collapse occurs at inter-transition timescales of order several weeks, although the precise threshold varies spatially across the MIZ. The broad interquartile range at short transition timescales reflects substantial variability associated with intermittently forced regimes near the ice edge, whereas longer transition times are associated with sustained, dynamically stable regimes. Together, panels (c) and (d) indicate that mixing regime instability in the MIZ is governed by transient, event-driven forcing and precedes changes in MIZ extent. This phase offset indicates that regime instability is driven by the rate of ice and surface forcing evolution rather than by MIZ extent itself, with dynamically active transition periods dominating mixing regime variability.

Figure 4 provides complementary information into how both local and spatially aggregated values of La_t, depend on sea ice concentration (SIC), and helps contextualize the spatial regime structure identified in Figure 3. Panel (a) shows that median La_t increases with SIC across most seasons, indicating a systematic shift toward shear-dominated conditions as ice cover increases. Conditions associated with strong LT potential ($La_t < 0.43$) are largely confined to OW or low SIC, whereas shear-dominated regimes ($La_t > 0.94$) prevail at moderate to high SIC. This behavior is consistent with the increasing attenuation of wave energy and reduction of Stokes drift under partial ice cover. During summer, however, median La_t exhibits a reduction at high SIC. This deviation is consistent with seasonal changes in ice mechanical properties and surface forcing, under which thinner and more fragmented ice with enhanced floe-scale heterogeneity may permit intermittent penetration of long-period swell into regions that remain nominally ice covered (Ardhuin et al., 2016; Brenner and Horvat, 2024). At the same time, wind stress over melting ice tends to be reduced and spatially variable, which can diminish shear-driven turbulence relative to wave-driven contributions. Within this context, the observed decrease in La_t at high SIC is interpreted as evidence for episodic wave influence under summer ice conditions, indicating that SIC alone does not uniquely constrain the wave impact on upper-ocean turbulence during the melt season. Panel (b) highlights the local variability of La_t using histograms of the minimum, mean, and maximum values computed over local 3×3 grid-cell neighborhoods. These neighborhood diagnostics are introduced to characterize the local dynamical environment experienced by each MIZ grid cell. The minimum value, $La_t^{\min}$, identifies the most wave-influenced neighboring point and provides an upper bound on local wave impact, while $La_t^{\max}$ reflects the most shear-dominated condition in the vicinity. The neighborhood mean, La_t^{mean}, closely tracks the single-grid-cell La_t, representing the dominant local regime, whereas the extremes reveal local scale variability that is masked by spatial averaging. Together, these distributions demonstrate that mixing regimes within the MIZ arise not only from seasonal modulation of SIC but also from strong spatial heterogeneity in wave and shear forcing at scales smaller than the model grid. This scale dependence suggests that conventional one-dimensional upper-ocean boundary layer parameterizations may inadequately represent mixing processes under partial ice cover, motivating the use of regime-based or local scale-aware approaches in ice–ocean models.

3.4 Pan-Arctic dissipation rates and seasonality

Figure 5 provides energetic context for the regime instability patterns identified in Figures 3–4 by explicitly characterizing both the magnitude and intermittency of mechanically driven upper-ocean dissipation under partial ice cover. Panel (a) shows the spatial distribution of median mechanical dissipation over 2018–2022 for SIC ≥ 0.15. Persistent dissipation is concentrated

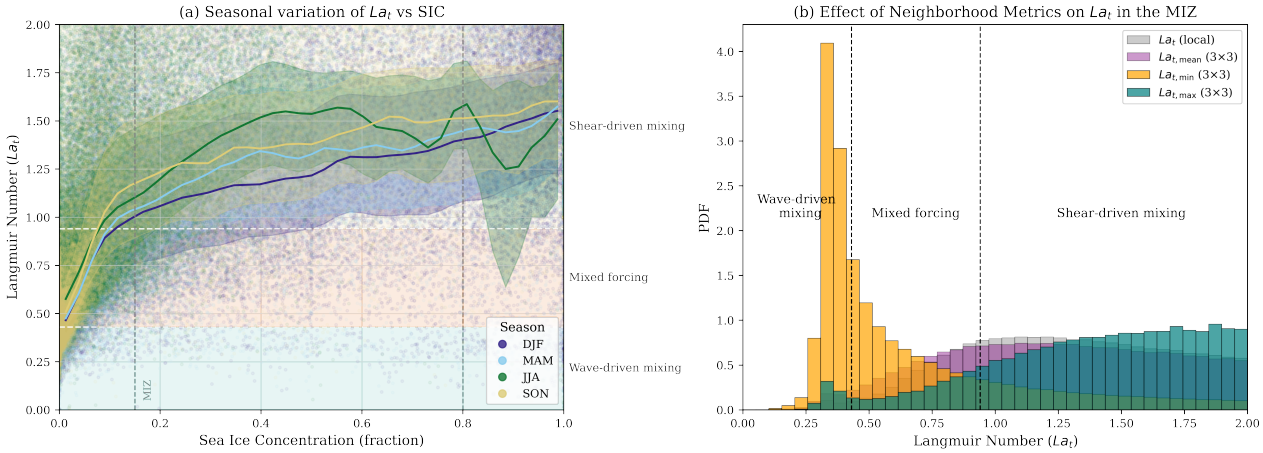

Figure 4. Sea ice concentration dependence of the turbulent Langmuir number. (**Left**) Parametric plot of La_t against binned sea ice concentration (SIC). Solid lines denote the median La_t for each season and bin, with shading indicating inter-quartile ranges. The white dashed lines mark the wave-dominated ($La_t < 0.43$) and shear-dominated ($La_t > 0.94$) regime thresholds. (**Right**) Normalized histogram of La_t values in each smoothing category, aggregated over all ice-covered grid cells (SIC ≥ 0.15). This histogram highlights the asymmetry and variability in the spatial scale and intensity of Langmuir turbulence across the Arctic.

along the marginal ice zone, wave-exposed shelves, and the seasonal ice edge, while the interior pack ice exhibits weak and spatially uniform dissipation. This pattern reflects the long-term background structure of mechanical energy input and identifies regions where wind–wave forcing recurrently couples to the upper ocean. Panel (b) reveals a complementary aspect of the forcing environment by mapping dissipation intermittency, quantified as log_10 (P90/median). High intermittency is strongly localized to narrow MIZ regions and ice edge corridors, indicating that dissipation in these areas is dominated by episodic events rather than sustained forcing. In contrast, regions with elevated median dissipation but low intermittency experience comparatively steady energy input. The close spatial correspondence between highly intermittent dissipation and previously identified regime-transition hotspots demonstrates that frequent mixing-regime changes arise preferentially where competing wind-, wave-, and ice-mediated processes alternately dominate on short timescales. The Arctic-wide time series in panel (c) further emphasizes the event-driven nature of mechanical dissipation, with variability dominated by intermittent extremes superimposed on a low median background. The large interquartile range relative to the median indicates that rare, high-energy events contribute disproportionately to temporal variability, consistent with the episodic forcing implied by the intermittency index. Panel (d) shows that this intermittency is seasonally modulated, with dissipation peaking during late summer and early autumn when ice cover is thinning and wave penetration is enhanced, and reaching a minimum during late winter under consolidated ice.

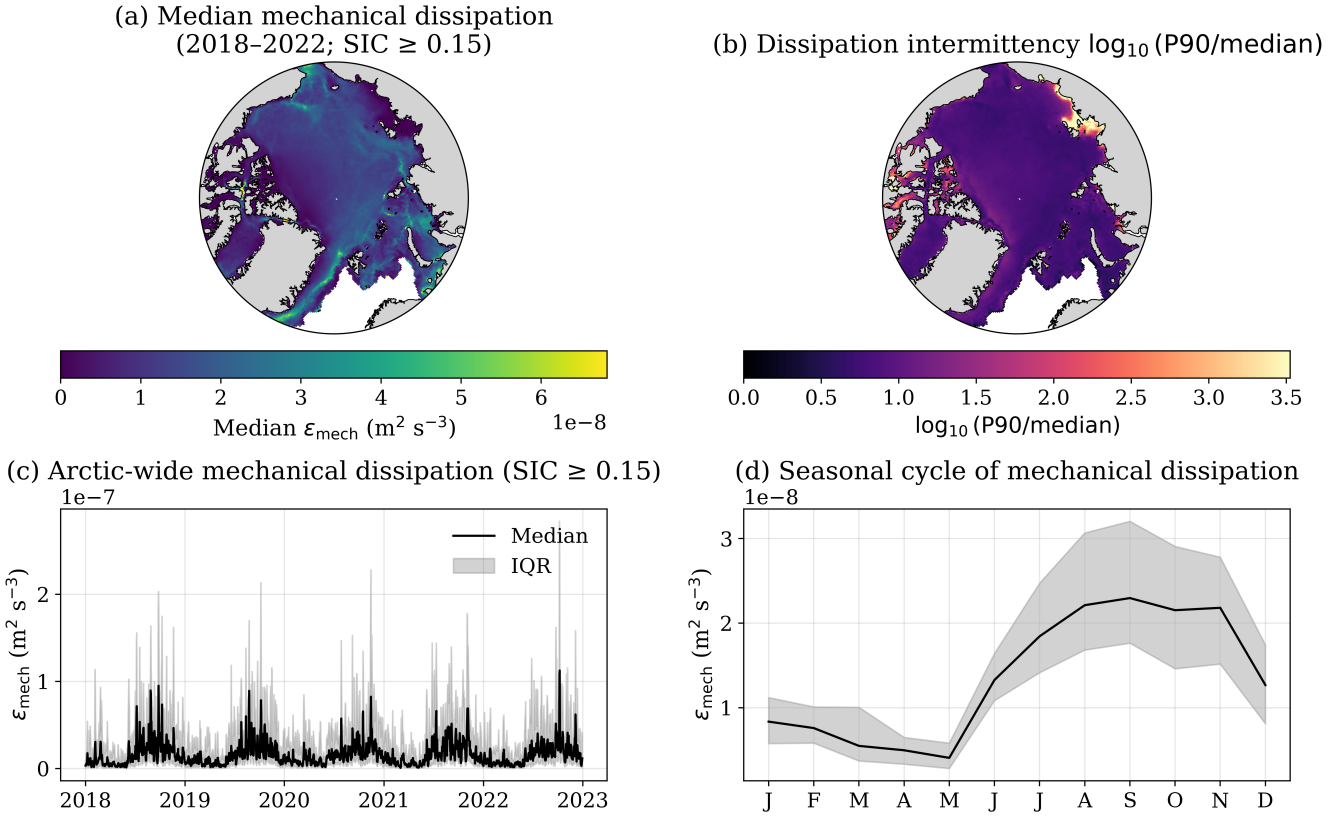

Figure 5. Mechanical dissipation magnitude and intermittency within the Arctic marginal ice zone (2018–2022). (a) Spatial distribution of the aggregated median mechanically forced dissipation, $\varepsilon_{\mathrm{mech}}$, evaluated for ice-covered conditions (SIC $\geq$ 0.15). **(b)** Dissipation intermittency index, defined as $\log_{10}(\mathrm{P90/median})$ of $\varepsilon_{\mathrm{mech}}$. **(c)** Arctic-wide temporal evolution of mechanically forced dissipation aggregated over all grid cells classified as MIZ (SIC $\geq$ 0.15), shown as the spatial median (black line) with interquartile range (shading), illustrating the strongly intermittent nature of MIZ energy input. **(d)** Seasonal cycle of mechanically forced dissipation within the MIZ, constructed from the monthly climatology of the spatial median in panel (c), with shading indicating the interquartile range.

3.5 Impact of wind–wave misalignment on Langmuir turbulence efficiency

While Figure 5 demonstrates that mechanically driven dissipation in the MIZ is highly intermittent and dominated by episodic events, the extent to which wave-induced forcing contributes to vertical mixing depends critically on the relative alignment of wind and waves. To isolate the role of wind–wave geometry in modulating Langmuir-driven mixing, we explicitly compare wind-aligned and dynamically projected Langmuir diagnostics using both local time series and pan-Arctic statistics. This analysis distinguishes between the *existence* of Langmuir forcing, as indicated by the turbulent Langmuir number La_t, and the *efficiency* with which that forcing is converted into vertical motions under realistic wind–wave alignment.

Because wind–wave misalignment is a local geometric property of the surface forcing rather than a spatially averaged quantity, all misalignment diagnostics are evaluated at the native model grid scale. Spatial smoothing does not qualitatively alter the inferred suppression of Langmuir-driven vertical motions, but it obscures the episodic nature of misalignment events and is therefore avoided here.

We first illustrate the impact of wind–wave misalignment using time series extracted at two dynamically contrasting locations representative of (i) the seasonal MIZ and (ii) the consolidated central Arctic (Figure 6). For each site, we show the standard La_t, the projected Langmuir number accounting for dynamically oriented Langmuir cells (La_{proj}), the mixed-layer-averaged vertical velocity variance $\langle w'^2 \rangle_{H_{\mathrm{ML}}}$ estimated from LES-based scalings, and daily sea ice concentration (SIC). Together, these metrics allow direct comparison between the potential for Langmuir forcing and its realized efficiency under evolving wind–wave alignment.

At the MIZ site, both La_t and La_{proj} exhibit pronounced seasonal variability associated with the expansion of the ice cover. Periods of reduced SIC permit wave penetration and enhanced Stokes drift, leading to episodic transitions into mixed- and wave-driven forcing regimes. During these intervals, La_{proj} is frequently lower than La_t, reflecting geometric suppression of Langmuir forcing due to wind–wave misalignment. These misalignment events coincide with elevated VKE, indicating that LT is energetically active but occurs at reduced efficiency relative to a wind-aligned reference state. In contrast, periods of high SIC are characterized by weak VKE and little distinction between La_t and La_{proj}, consistent with strong wave attenuation beneath the ice cover.

The central Arctic site exhibits markedly different behavior. Persistently high SIC limits wave penetration throughout most of the year, resulting in consistently large Langmuir numbers and weak VKE. Differences between La_t and La_{proj} are small and infrequent, indicating that wind–wave misalignment plays a secondary role where wave-induced Stokes drift is already strongly suppressed. Even when brief reductions in SIC occur, the associated misalignment produces only modest changes in VKE due to the overall lack of energetic wave forcing.

These local time series demonstrate that wind–wave misalignment does not determine whether LT is present, but rather modulates its efficiency when wave-driven forcing is active. Misalignment effects are therefore most pronounced in the MIZ, where partial ice cover allows wave penetration and energetic Langmuir motions, while they remain muted in the consolidated central Arctic. This motivates a broader, pan-Arctic assessment of misalignment-driven suppression of LT efficiency, which we quantify below using a non dimensional efficiency metric.

To quantify the impact of wind–wave misalignment across the Arctic, we define the ratio

$$R_{LT} = \langle w'^2 \rangle_{La_{\mathrm{proj}}} / \langle w'^2 \rangle_{La_t},$$

which measures the efficiency of Langmuir-driven vertical motions relative to a wind-aligned reference state. Here, R_{LT} is interpreted as an efficiency factor: values near unity indicate that Langmuir-driven vertical motions approach their wind-aligned maximum, while lower values quantify the fraction of Langmuir potential lost due to wind–wave misalignment.

Figure 7a shows that R_{LT} decreases systematically with increasing Langmuir cell orientation angle α_{LOW}, demonstrating a progressive suppression of VKE as wind–wave alignment deteriorates. R_{LT} approaches unity only under near-perfect

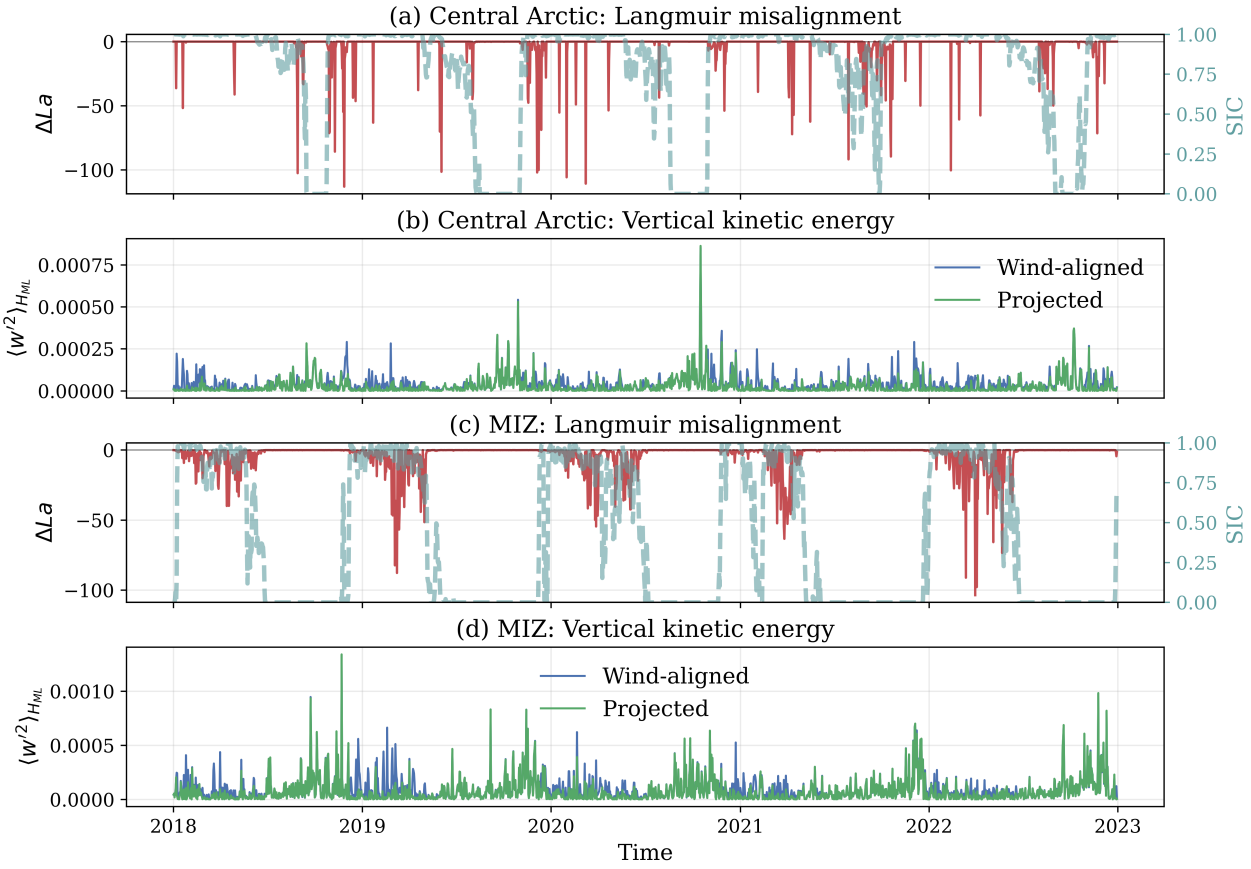

Figure 6. Impact of wind–wave misalignment on Langmuir turbulence at representative Arctic sites. Time series extracted at a consolidated central Arctic location (**a,b**) and a seasonal MIZ location (**c,d**). Panels **(a)** and **(c)** show the Langmuir misalignment metric $\Delta La = La_{\mathrm{proj}} - La_t$, where La_t is the wind-aligned turbulent Langmuir number and La_{proj} accounts for dynamically projected Langmuir cell orientation. Negative values indicate geometric suppression of Langmuir forcing due to wind–wave misalignment. Sea ice concentration (SIC) is overlaid on a secondary axis (dashed teal line). Panels **(b)** and **(d)** show the mixed-layer-averaged vertical velocity variance $\langle w'^2 \rangle_{H_{\mathrm{ML}}}$ estimated from LES-based scalings, comparing wind-aligned (blue) and projected (green) Langmuir forcing.

alignment and does not exceed unity, confirming that Langmuir cell rotation acts as a purely geometric limiter rather than an amplifying mechanism. Across the MIZ, wind–wave misalignment typically reduces Langmuir-induced vertical velocity variance by 30–50% relative to wind-aligned estimates, with stronger suppression during shear-dominated conditions. Recasting the same relationship in terms of $\cos^2(\alpha_{\mathrm{LOW}})$ reveals a near-collapse of R_{LT} across shear-dominated, mixed-forcing, and wave-dominated regimes (Figure 7b). In all regimes, Langmuir efficiency closely follows the ideal geometric scaling $R_{LT} =$

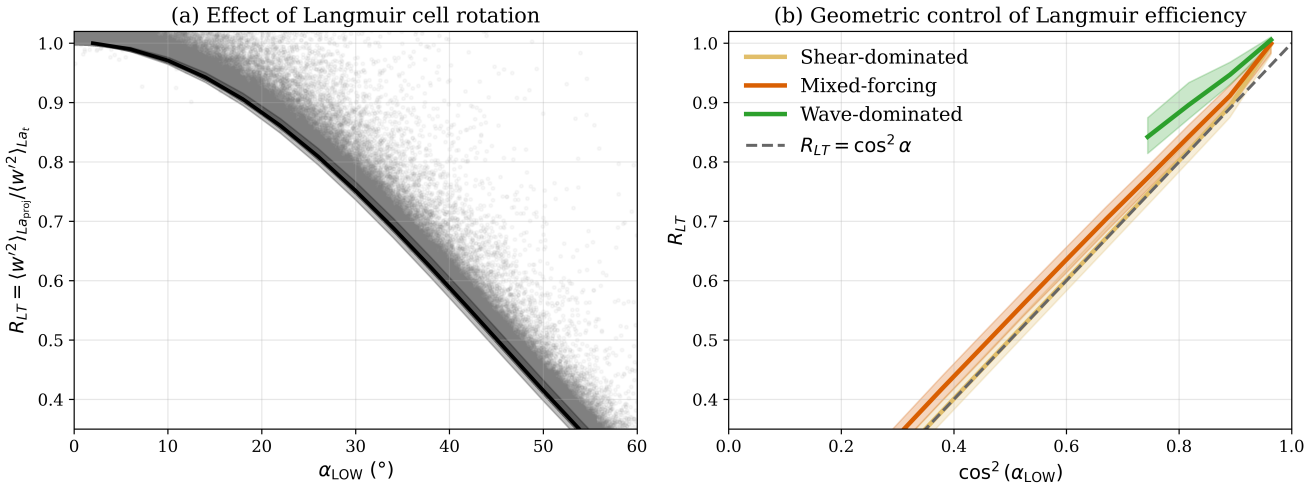

Figure 7. Geometric control of Langmuir turbulence efficiency by wind–wave misalignment. (**a**) Dependence of the Langmuir efficiency factor $R_{LT} = \langle w'^2 \rangle_{La_{\mathrm{proj}}} / \langle w'^2 \rangle_{La_t}$ on the Langmuir cell orientation angle α_{LOW} for all ice-covered grid cells. Gray points show individual grid–time samples, while the black curve and shading denote the binned median and interquartile range. (**b**) Same data recast as a function of $\cos^2(\alpha_{\mathrm{LOW}})$, highlighting the underlying geometric control on Langmuir efficiency. Colored curves show regime-conditioned medians for shear-dominated, mixed-forcing, and wave-dominated regimes, with shaded envelopes indicating interquartile ranges. The dashed line denotes the ideal geometric scaling $R_{LT} = \cos^2 \alpha$.

$\cos^2 \alpha$, with regime-dependent offsets reflecting differences in baseline forcing rather than changes in functional behavior. This collapse demonstrates that wind–wave alignment primarily controls the *efficiency* with which Langmuir forcing is converted into vertical motions, while the underlying forcing regime governs the available Langmuir potential.

Across all MIZ grid cells ($0.15 \leq \mathrm{SIC} \leq 0.8$), the median value of R_{LT} is 0.84, with an interquartile range of 0.34–1.00, indicating that wind–wave misalignment generally produces modest suppression of Langmuir-driven vertical velocity variance, while occasionally reducing it by more than 60% during strongly misaligned events. The full distribution of R_{LT} across the MIZ is shown in Supplemental Fig. S3. Wind–wave misalignment therefore emerges as a physically robust, regime-independent geometric modulator of Langmuir turbulence efficiency when wave-driven forcing is active in the Arctic, distinct from variations in the local wave–shear balance.

4 Discussion and Conclusions

4.1 The marginal ice zone as a dynamically distinct mixing regime

Our results demonstrate that surface forcing capable of sustaining Langmuir turbulence (LT) in the Arctic is both spatially confined and temporally intermittent. Conditions resembling open-water wind–wave forcing occur predominantly within the

seasonal marginal ice zone (MIZ), while the interior pack ice remains largely shear dominated. Even within the MIZ, joint exceedance of wind stress and Stokes drift rarely exceeds 20% of the time, indicating that LT beneath ice is not a persistent background process but instead emerges episodically.

A pronounced seasonal asymmetry further characterizes this behavior. Despite the largest spatial extent of the MIZ during summer, LT-relevant forcing and Langmuir enhancement are weakest in this season. This counterintuitive result reflects the competing effects of ice retreat and wave attenuation: moderate ice concentrations efficiently damp Stokes drift, consistent with theoretical and observational studies documenting rapid decay of wave energy and Stokes transport under partial ice cover (Liu and Mollo-Christensen, 1988; Ardhuin et al., 2016; Herman, 2017), while summer winds tend to be weaker and less coherent. As a result, expanded MIZ area does not translate into enhanced LT activity.

In contrast, winter and transitional seasons exhibit more frequent and spatially coherent open-water–like forcing along the evolving ice edge. During these periods, episodic storms generate strong winds and long-period swell that can temporarily overcome wave attenuation and penetrate into the MIZ (Thomson, 2022; Boutin et al., 2022). These events produce brief but dynamically significant excursions toward low La_t, enhanced mechanical dissipation, and elevated LT efficiency. Taken together, our results show that the seasonal imprint of LT in the Arctic is governed by the intensity and coherence of wind–wave forcing rather than by MIZ extent alone. This finding is consistent with conceptual views of the MIZ as a dynamically active wave–ice interaction zone rather than a purely geometric transition region (Squire and Williams, 2008; Horvat and Tziperman, 2015).

4.2 Sea ice regulation of Stokes drift and Langmuir turbulence potential

Across all diagnostics, sea ice concentration (SIC) emerges as a first-order regulator of the *mean* balance between wave- and shear-driven turbulence. For most seasons, median La_t increases monotonically with SIC, reflecting progressive suppression of Stokes drift relative to wind stress as ice cover increases. Consequently, the central Arctic is characterized by persistently shear-dominated conditions, long regime persistence, and weak variability in LT-related metrics.

Departures from this monotonic relationship during summer, most notably reduced La_t at higher SIC, do not indicate sustained wave forcing within the interior pack. Instead, they reflect intermittent wave penetration enabled by thinner, more fragmented ice and enhanced floe-scale heterogeneity during the melt season. Under these conditions, long-period swell can episodically access regions that remain nominally ice covered, temporarily reducing La_t without establishing a persistent wave-driven regime. These results highlight that while SIC controls the background forcing state, the mechanical properties of the ice and the spectral characteristics of the wave field modulate the realization of wave influence in ways not captured by concentration alone.

4.3 Forcing intermittency, regime instability, and Langmuir efficiency

The regime-based analysis further reveals that the MIZ is not merely a spatial transition zone but a dynamically distinct environment characterized by enhanced variability and frequent reorganization of surface forcing. Regime instability peaks when grid cells reside near thresholds separating shear-, mixed-, and wave-dominated regimes, rather than when the MIZ is

most extensive. Periods of broad MIZ coverage are often dynamically stable, whereas narrow, rapidly evolving ice edges promote frequent regime switching. This behavior extends earlier work showing that ice-edge variability is governed by dynamical thresholds rather than ice extent alone (Horvat et al., 2016).

Energetic diagnostics indicate that this instability is driven primarily by the intermittency of mechanical dissipation rather than by its mean magnitude. Highly intermittent dissipation is strongly localized to the same MIZ corridors that exhibit frequent regime transitions, demonstrating that episodic forcing events associated with storms and wave penetration dominate the dynamical evolution of the system. This finding aligns with broader evidence that turbulent mixing in both open-ocean and ice-covered environments is controlled by intermittent, high-energy events rather than by time-mean forcing (Belcher et al., 2012; McWilliams, 2016; Ardhuin et al., 2016; Thomson, 2022; Boutin et al., 2022).

Explicitly accounting for wind–wave misalignment further refines the diagnosis of Langmuir-driven mixing. Comparisons between wind-aligned and dynamically projected Langmuir diagnostics show that misalignment acts as a systematic geometric constraint on LT efficiency by reducing the effective Stokes shear projected onto the Langmuir cell axis. This behavior is consistent with theoretical and large-eddy simulation studies demonstrating that Langmuir turbulence intensity depends not only on the magnitude of Stokes drift but also on its orientation relative to the wind stress (McWilliams et al., 1997; Harcourt and D'Asaro, 2008; Harcourt, 2015; Van Roekel et al., 2012). Increasing misalignment suppresses vertical velocity variance even when wave forcing is present.

In our analysis, wind–wave misalignment reduces the realized contribution of LT to vertical mixing across all surface forcing regimes without altering the underlying regime classification. Thus, while La_t determines whether Langmuir forcing is present, geometric alignment governs how efficiently that forcing is converted into vertical motions. Together, our results demonstrate that LT in the Arctic is highly heterogeneous in space and time, responding dynamically to variations in waves, sea ice, and wind geometry. The MIZ emerges as the primary region where intermittent forcing, geometric constraints, and competing production mechanisms interact, underscoring the need for regime-aware and geometry-aware representations of upper-ocean mixing under partial ice cover.

4.4 Limitations and Future Directions

Our approach is based on bulk diagnostics and empirically derived scalings and therefore carries several important limitations. The use of $\sim$25 km resolution fields limits our ability to resolve fine-scale processes such as mesoscale and submesoscale eddies, floe-scale wave attenuation, and narrow leads and polynyas, all of which can locally modulate Langmuir turbulence and upper-ocean mixing. Although neighborhood-based statistics partially capture local heterogeneity, direct assessment of small-scale Langmuir dynamics ultimately requires higher-resolution modeling and targeted *in situ* observations.

In addition, our analysis relies on a coupled sea ice–wave framework in which the ocean mixed layer does not respond dynamically to wind–wave forcing and explicit ocean stratification feedbacks are not resolved. Mixed-layer depth and buoyancy effects are therefore prescribed rather than prognostic, constraining the realism of the diagnosed vertical mixing response. In particular, buoyancy-driven convection and Langmuir turbulence are expected to interact nonlinearly in ice-covered and meltwater-influenced environments, yet their relative contributions remain poorly constrained in the present framework. As a

result, the diagnostics presented here should be interpreted as indicators of Langmuir *potential* rather than as predictions of realized turbulent states.

4.4.1 Implications for ocean and climate modeling.

Despite these limitations, our results provide several clear implications for the representation of upper-ocean mixing under partial ice cover in climate and Earth system models. First, the strong intermittency and regime dependence of Langmuir turbulence in the MIZ imply that parameterizations based on time-mean forcing or sea ice concentration alone are unlikely to capture the episodic nature of mechanically driven mixing. Instead, regime-aware formulations that respond to joint wind–wave conditions and their temporal variability are required.

Second, our analysis demonstrates that wind–wave misalignment acts as a systematic geometric limiter on LT efficiency, independent of the underlying wave–shear balance. This finding suggests that existing Langmuir parameterizations, which often assume wind-aligned Stokes drift, may systematically overestimate vertical mixing in partially ice-covered regions unless geometric effects are explicitly accounted for. Incorporating misalignment-aware scaling factors or projected Stokes drift formulations offers a physically grounded pathway for improving LT representations without substantially increasing model complexity.

Finally, the spatial confinement of LT-relevant forcing to narrow, evolving MIZ corridors highlights the need for parameterizations that are robust across sharp transitions in surface state. In coarse-resolution models, where the MIZ is often poorly resolved, neglecting this spatial and temporal localization may lead to either excessive mixing within the interior pack or insufficient mixing near the ice edge. Our results therefore motivate the development of scale-aware and regime-based mixing schemes that adapt dynamically to ice concentration, wave exposure, and wind–wave geometry.

Addressing these challenges ultimately requires fully coupled ocean–wave–ice models that resolve stratification, wave propagation beneath ice, and wind–wave misalignment simultaneously. Recent and ongoing studies are beginning to resolve Langmuir turbulence under partially ice-covered and weakly stratified regimes using large-eddy simulations, regional modeling, and coordinated observations (e.g., Brenner et al., 2023; Lee et al., 2025). These efforts provide a clear pathway toward stratification-aware, ice-modified Langmuir parameterizations.

Complementary observational efforts are also essential. Coordinated field campaigns employing autonomous profilers, SWIFT drifters, and satellite altimetry will be critical for evaluating Langmuir diagnostics and parameterizations in ice-covered waters. In particular, observational and modeling studies should prioritize the MIZ, where wave–ice–wind interactions are most dynamically active. Finally, quantifying the impact of Langmuir turbulence on vertical tracer transport, stratification erosion, and ice–ocean heat exchange in climate models will be essential for assessing its broader role in the evolving Arctic system.

. The model outputs and post-processed Langmuir turbulence diagnostics used in this study are publicly available via Zenodo at https://zenodo.org/records/17372007. Analysis scripts are hosted on GitHub at https://github.com/atavri/Langmuir_turbulence_Arctic.git. ERA5

atmospheric reanalysis data are available from the Copernicus Climate Data Store, and the GLORYS12V1 ocean reanalysis is available through the Copernicus Marine Service.

. A.T. led the study, including conceptualization, analysis, and writing of the original draft. C.H., B.P., and A.T. contributed to interpretation of results and manuscript review and editing. G.B. contributed to model data curation and technical support. A.H. and A.K. contributed to early analysis and scientific discussion.

. The authors declare that they have no competing interests.

. This research was supported in part by the National Science Foundation (NSF OPP-2146910 and OCE-2148655) and by Schmidt Sciences, LLC through the SASIP project. The simulations were performed using resources provided by Sigma2—the National Infrastructure for High-Performance Computing and Data Storage in Norway.

We thank Sam Brenner for their assistance during the project initialization phase and for insightful discussions that helped shape the use of the Langmuir turbulence parameterizations.

References

Ali, A., Christensen, K. H., Breivik, Ø., Malila, M., Raj, R. P., Bertino, L., Chassignet, E. P., and Bakhoday-Paskyabi, M.: A comparison of Langmuir turbulence parameterizations and key wave effects in a numerical model of the North Atlantic and Arctic Oceans, Ocean Modelling, 137, 76–97, 2019.

Ardhuin, F., Sutherland, P., Doble, M., and Wadhams, P.: Ocean waves across the Arctic: Attenuation due to dissipation dominates over scattering for periods longer than 19 s, Geophysical Research Letters, 43, 5775–5783, 2016.

Ardhuin, F., Boutin, G., Stopa, J., Girard-Ardhuin, F., Melsheimer, C., Thomson, J., Kohout, A., Doble, M., and Wadhams, P.: Wave attenuation through an Arctic marginal ice zone on 12 October 2015: 2. Numerical modeling of waves and associated ice breakup, Journal of Geophysical Research: Oceans, 123, 5652–5668, 2018.

Ardhuin, F., Otero, M., Merrifield, S., Grouazel, A., and Terrill, E.: Ice breakup controls dissipation of wind waves across southern ocean sea ice, Geophysical Research Letters, 47, e2020GL087 699, 2020.

Armitage, T. W., Bacon, S., Ridout, A. L., Petty, A. A., Wolbach, S., and Tsamados, M.: Arctic Ocean surface geostrophic circulation 2003–2014, The Cryosphere, 11, 1767–1780, 2017.

Belcher, S. E., Grant, A. L., Hanley, K. E., Fox-Kemper, B., Van Roekel, L., Sullivan, P. P., Large, W. G., Brown, A., Hines, A., Calvert, D., et al.: A global perspective on Langmuir turbulence in the ocean surface boundary layer, Geophysical Research Letters, 39, 2012.

Boutin, G., Ardhuin, F., Dumont, D., Sévigny, C., Girard-Ardhuin, F., and Accensi, M.: Floe size effect on wave-ice interactions: Possible effects, implementation in wave model, and evaluation, Journal of Geophysical Research: Oceans, 123, 4779–4805, 2018.

Boutin, G., Lique, C., Ardhuin, F., Rousset, C., Talandier, C., Accensi, M., and Girard-Ardhuin, F.: Towards a coupled model to investigate wave–sea ice interactions in the Arctic marginal ice zone, The Cryosphere, 14, 709–735, 2020.

Boutin, G., Williams, T., Rampal, P., Olason, E., and Lique, C.: Wave–sea-ice interactions in a brittle rheological framework, Cryosphere, 15, 431–457, 2021.

Boutin, G., Williams, T., Horvat, C., and Brodeau, L.: Modelling the Arctic wave-affected marginal ice zone: a comparison with ICESat-2 observations, Philosophical Transactions of the Royal Society A, 380, 20210 262, 2022.

Brenner, S. and Horvat, C.: Scaling simulations of local wind-waves amid sea ice floes, Journal of Geophysical Research: Oceans, 129, e2024JC021 629, 2024.

Brenner, S., Rainville, L., Thomson, J., Cole, S., and Lee, C.: Comparing observations and parameterizations of ice-ocean drag through an annual cycle across the Beaufort Sea, Journal of Geophysical Research: Oceans, 126, e2020JC016 977, 2021.

Brenner, S., Horvat, C., Hall, P., Lo Piccolo, A., Fox-Kemper, B., Labbé, S., and Dansereau, V.: Scale-dependent air-sea exchange in the polar oceans: Floe-floe and floe-flow coupling in the generation of ice-ocean boundary layer turbulence, Geophysical Research Letters, 50, e2023GL105 703, 2023.

Collins, C., Doble, M., Lund, B., and Smith, M.: Observations of surface wave dispersion in the marginal ice zone, Journal of Geophysical Research: Oceans, 123, 3336–3354, 2018.

Cooper, V. T., Roach, L., Thomson, J., Brenner, S., Smith, M., Meylan, M., and Bitz, C.: Wind waves in sea ice of the western Arctic and a global coupled wave-ice model, Philosophical Transactions of the Royal Society A, 380, 20210 258, 2022.

Craik, A. D. and Leibovich, S.: A rational model for Langmuir circulations, Journal of Fluid Mechanics, 73, 401–426, 1976.

D'Asaro, E. A.: Turbulence in the upper-ocean mixed layer, Annual review of marine science, 6, 101–115, 2014.

Dethleff, D. and Kempema, E.: Langmuir circulation driving sediment entrainment into newly formed ice: Tank experiment results with application to nature (Lake Hattie, United States; Kara Sea, Siberia), Journal of Geophysical Research: Oceans, 112, 2007.

Dosser, H. V. and Rainville, L.: Dynamics of the changing near-inertial internal wave field in the Arctic Ocean, Journal of Physical Oceanography, 46, 395–415, 2016.

Drucker, R., Martin, S., and Moritz, R.: Observations of ice thickness and frazil ice in the St. Lawrence Island polynya from satellite imagery, upward looking sonar, and salinity/temperature moorings, Journal of Geophysical Research: Oceans, 108, 2003.

Gargett, A. and Grosch, C.: Turbulence process domination under the combined forcings of wind stress, the Langmuir vortex force, and surface cooling, Journal of Physical Oceanography, 44, 44–67, 2014.

Harcourt, R. R.: An improved second-moment closure model of Langmuir turbulence, Journal of Physical Oceanography, 45, 84–103, 2015.

Harcourt, R. R. and D'Asaro, E. A.: Large-eddy simulation of Langmuir turbulence in pure wind seas, Journal of Physical Oceanography, 38, 1542–1562, 2008.

Herman, A.: Wave-induced stress and breaking of sea ice in a coupled hydrodynamic discrete-element wave–ice model, The Cryosphere, 11, 2711–2725, 2017.

Horvat, C. and Tziperman, E.: A prognostic model of the sea-ice floe size and thickness distribution, The Cryosphere, 9, 2119–2134, 2015.

Horvat, C., Tziperman, E., and Campin, J.-M.: Interaction of sea ice floe size, ocean eddies, and sea ice melting, Geophysical Research Letters, 43, 8083–8090, 2016.

Horvat, C., Blanchard-Wrigglesworth, E., and Petty, A.: Observing waves in sea ice with ICESat-2, Geophysical Research Letters, 47, e2020GL087 629, 2020.

Kirillov, S. A., Dmitrenko, I. A., Hölemann, J. A., Kassens, H., and Bloshkina, E.: The penetrative mixing in the Laptev Sea coastal polynya pycnocline layer, Continental Shelf Research, 63, 34–42, 2013.

Kukulka, T., Plueddemann, A. J., Trowbridge, J. H., and Sullivan, P. P.: Rapid mixed layer deepening by the combination of Langmuir and shear instabilities: A case study, Journal of Physical Oceanography, 40, 2381–2400, 2010.

Kukulka, T., Plueddemann, A. J., and Sullivan, P. P.: Inhibited upper ocean restratification in nonequilibrium swell conditions, Geophysical Research Letters, 40, 3672–3676, 2013.

Lee, A., Hutchings, J., Horvat, C., Tavri, A., and Pearson, B.: Impact of Surface Waves on Mixing and Circulation in a Summertime Lead, EGUsphere, 2025, 1–33, 2025.

Leibovich, S.: The form and dynamics of Langmuir circulations, Annual review of fluid mechanics, 15, 391–427, 1983.

Li, Q. and Fox-Kemper, B.: Assessing the effects of Langmuir turbulence on the entrainment buoyancy flux in the ocean surface boundary layer, Journal of Physical Oceanography, 47, 2863–2886, 2017.

Li, Q., Reichl, B. G., Fox-Kemper, B., Adcroft, A. J., Belcher, S. E., Danabasoglu, G., Grant, A. L., Griffies, S. M., Hallberg, R., Hara, T., et al.: Comparing ocean surface boundary vertical mixing schemes including Langmuir turbulence, Journal of Advances in Modeling Earth Systems, 11, 3545–3592, 2019.

Liu, A. K. and Mollo-Christensen, E.: Wave propagation in a solid ice pack, Journal of physical oceanography, 18, 1702–1712, 1988.

Lo Piccolo, A., Horvat, C., and Fox-Kemper, B.: Energetics and Transfer of Submesoscale Brine-Driven Eddies at a Sea Ice Edge, Journal of Physical Oceanography, 54, 1489–1501, 2024.

Manucharyan, G. E. and Thompson, A. F.: Submesoscale sea ice-ocean interactions in marginal ice zones, Journal of Geophysical Research: Oceans, 122, 9455–9475, 2017.

McWilliams, J. C.: Submesoscale currents in the ocean, Proceedings of the Royal Society A: Mathematical, Physical and Engineering Sciences, 472, 20160 117, 2016.

McWilliams, J. C. and Sullivan, P. P.: Vertical mixing by Langmuir circulations, Spill Science & Technology Bulletin, 6, 225–237, 2000.

McWilliams, J. C., Sullivan, P. P., and Moeng, C.-H.: Langmuir turbulence in the ocean, Journal of Fluid Mechanics, 334, 1–30, 1997.

Morison, J. H., Long, C. E., and Levine, M. D.: Internal wave dissipation under sea ice, Journal of Geophysical Research: Oceans, 90, 11 959–11 966, 1985.

Muilwijk, M., Hattermann, T., Martin, T., and Granskog, M. A.: Future sea ice weakening amplifies wind-driven trends in surface stress and Arctic Ocean spin-up, Nature Communications, 15, 6889, 2024.

Ólason, E., Boutin, G., Williams, T., Korosov, A., Regan, H., Rheinlænder, J., Rampal, P., Flocco, D., Samaké, A., Davy, R., et al.: The next generation sea-ice model neXtSIM, version 2, EGUsphere, 2025, 1–33, 2025.

Pearson, B. C., Grant, A. L., Polton, J. A., and Belcher, S. E.: Langmuir turbulence and surface heating in the ocean surface boundary layer, Journal of Physical Oceanography, 45, 2897–2911, 2015.

Pinkel, R.: Near-inertial wave propagation in the western Arctic, Journal of physical oceanography, 35, 645–665, 2005.

Polton, J. A. and Belcher, S. E.: Langmuir turbulence and deeply penetrating jets in an unstratified mixed layer, Journal of Geophysical Research: Oceans, 112, 2007.

Rainville, L., Lee, C. M., and Woodgate, R. A.: Impact of wind-driven mixing in the Arctic Ocean, Oceanography, 24, 136–145, 2011.

Rampal, P., Bouillon, S., Ólason, E., and Morlighem, M.: neXtSIM: a new Lagrangian sea ice model, The Cryosphere, 10, 1055–1073, 2016.

Skyllingstad, E. D. and Denbo, D. W.: An ocean large-eddy simulation of Langmuir circulations and convection in the surface mixed layer, Journal of Geophysical Research: Oceans, 100, 8501–8522, 1995.

Skyllingstad, E. D. and Denbo, D. W.: Turbulence beneath sea ice and leads: A coupled sea ice/large-eddy simulation study, Journal of Geophysical Research: Oceans, 106, 2477–2497, 2001.

Smyth, W. D., Skyllingstad, E. D., Crawford, G. B., and Wijesekera, H.: Nonlocal fluxes and Stokes drift effects in the K-profile parameterization, Ocean Dynamics, 52, 104–115, 2002.

Squire, V. and Williams, T.: Wave propagation across sea-ice thickness changes, Ocean Modelling, 21, 1–11, 2008.

Squire, V. A.: A fresh look at how ocean waves and sea ice interact, Philosophical Transactions of the Royal Society A: Mathematical, Physical and Engineering Sciences, 376, 20170 342, 2018.

Stopa, J. E., Ardhuin, F., and Girard-Ardhuin, F.: Wave climate in the Arctic 1992–2014: Seasonality and trends, The Cryosphere, 10, 1605–1629, 2016.

Sullivan, P. P., McWILLIAMS, J. C., and Melville, W. K.: Surface gravity wave effects in the oceanic boundary layer: Large-eddy simulation with vortex force and stochastic breakers, Journal of Fluid Mechanics, 593, 405–452, 2007.

Thomson, J.: Wave propagation in the marginal ice zone: connections and feedback mechanisms within the air–ice–ocean system, Philosophical Transactions of the Royal Society A, 380, 20210 251, 2022.

Thomson, J. and Rogers, W. E.: Swell and sea in the emerging Arctic Ocean, Geophysical Research Letters, 41, 3136–3140, 2014.

Tolman, H. L. et al.: User manual and system documentation of WAVEWATCH III TM version 3.14, Technical note, MMAB contribution, 276, 2009.

Van Roekel, L., Fox-Kemper, B., Sullivan, P., Hamlington, P., and Haney, S.: The form and orientation of Langmuir cells for misaligned winds and waves, Journal of Geophysical Research: Oceans, 117, 2012.

Voermans, J., Babanin, A., Thomson, J., Smith, M., and Shen, H.: Wave attenuation by sea ice turbulence, Geophysical Research Letters, 46, 6796–6803, 2019.

Webb, A. and Fox-Kemper, B.: Wave spectral moments and Stokes drift estimation, Ocean modelling, 40, 273–288, 2011.

Yang, D., Chamecki, M., and Meneveau, C.: Inhibition of oil plume dilution in Langmuir ocean circulation, Geophysical Research Letters, 41, 1632–1638, 2014.